Near-infrared circular dichroism of the ytterbium DOTMA complex: an ab initio investigation

Frédéric Gendron, Maxime Grasser, Boris Le Guennic

Near-Infrared Circular Dichroism of the Ytterbium DOTMA Complex: An Ab-initio Investigation

Frédéric Gendron,* [a] Maxime Grasser,[a] and Boris Le Guennic* [a]

[a] Univ Rennes, CNRS, ISCR (Institut des Sciences Chimiques de Rennes) UMR 6226, F-35000 Rennes, France

email: fredo.gendron@gmail.com, boris.leguennic@univ-rennes1.fr

December 20, 2021

Abstract

Electronic structure and circular dichroism spectra of the Ytterbium(III) complex $[Yb(DOTMA)]^-$ are calculated using complete and restricted active space self-consistent field wavefunction methods with the spin-orbit coupling treated by the state interaction approach. The influence of the dynamical correlation effect is then included via the 2nd order perturbation method. The experimental circular dichroism spectrum is well reproduced by the calculations, both in term of relative energy excitations and in term of rotatory strengths intensities. The results allow highlighting on the mechanism that drive the chiroptical properties in Yb(III) complexes and reveal the importance on taking into account the $4f^{12}5d^1$ electronic configurations in the calculated wavefunctions to properly describe the chiroptical properties of the $4f-4f$ transitions.

1 Introduction

The attention drawn to chiral lanthanide chemistry has raised significantly over the last two decades because of the large panel of applications that can be designed with the help of these compounds.[1] Among many applications, one may mention the use of chiral Ln(III)-based complexes as luminescente probes or as contrast agents in magnetic resonance imaging,[2–4] as security inks and anti-counterfeiting tags,[5,6] or as circularly polarized organic light-emitting diodes in display technology.[7,8] The origin of these appealing applications arises from the peculiar electronic structure of the Ln(III) centers and the presence of a partially-filled $4f$ shell[9,10] that gives rise to magnetic properties.[11–14] The associated inner-shell $4f-4f$ transitions are formally electric-dipole (ED) forbidden, preventing any optical activity. However, under the combined effects of the crystal-field (CF) interaction and the spin-orbit coupling (SOC), electronic transitions can gain ED intensities and hence, very narrow and well-defined absorption or emission bands can be experimentally observed. Moreover, the available spectral window can be modulated by switching the nature of the

Ln(III) ion as the coordination sphere remains very similar upon replacement of the metal center. For instance, the emission spectrum can be shifted from the ultra-violet with a Gd(III) ion, to visible with Eu(III), and to near-infrared (NIR) with Yb(III).[2] The NIR spectral region being particularly advantageous for medical applications as the biological tissues are transparent in this region.

Among chiral Yb(III)-based systems,[11,15–24] the circular dichroism (CD) spectra of the $[Yb(DOTMA)]^-$ [DOTMA = (1,R,4R,7R,10R)-α,α',α'',α'''-tetramethyl-1,4,7,10-tetraazacyclododecane-1,4,7,10-tetraacetic acid][25–27] was fully characterized in solution by Di Bari *et al.* in the early 2000s. The CD spectra presented well-resolved transitions around ca. 980 nm, which correspond to excitations from the ground level $^2F_{7/2}$ of the Yb(III) ion into the excited one $^2F_{5/2}$. Later on, mechanism at the origin of the optical activity for this complex was tentatively rationalized by Berardozzi[28] with the help of an electrostatic model[29,30] that combines CF theory and the semi-empirical Judd-Ofelt theory.[31,32] Interestingly, the dominant mechanism allowing the electronic transitions to gain ED intensities and hence rotational strength, was attributed to a *static-coupling* mechanism.[28] Here, *static-coupling* refers to the breaking of the parity rule of the wavefunction and arises in fully dissymmetric environment. Theoretically, it can be achieved by mixing the $4f^n$ configurations in the wavefunction with $4f^{n-1}5d$ and $4f^{n-1}ng$ configurations. On the other hand, the *dynamic-coupling* occurs when the electric quadrupole of the Ln(III) center induces an ED moment localized on the ligands, corresponding thus to ligand polarizability, and arises mostly with π-type ligands.[33] The choice of $[Yb(DOTMA)]^-$ is particularly suited to theoretically gain mechanism insight. Indeed, the experimental ECD spectrum was obtained in methanol and attributed to one major form which prevents direct solvent coordination on the Ytterbium center. The use of another solvent than methanol, could lead to a modification of the equilibrium between the major and minor forms, favoring the coordination of solvent molecule on the minor form. Such a direct coordination of a solvent molecule to the lanthanide center would strongly modify the electronic structure of the complex by changing the interaction of the crystal-field, and would result into a different CD spectrum. On a related complex, Di Bari *et al.* showed that the use of DMSO solvent instead of methanol led to axial coordination of the solvent which strongly altered the CD spectrum.[26]

To the best of our knowledge, no *ab-initio* calculations have ever been performed in order to calculate and rationalize the CD spectra associated to the $4f$ transitions in Ln(III) complexes. One can mention the use of Kohn-Sham time-dependent density functional theory to calculate the UV-CD spectra of the $[Yb(BINOLate)_3]^{3-}$ complex, but the investigated transitions corresponded to the ligand centered $\pi-\pi^*$ transitions.[34] So far, only electrostatic models with empirical parameters have been employed to simulate CD spectrum of $4f$ transitions.[28] The use of such models prevent from fully rationalizing the different mechanisms at the origin of the chiroptical activity, particularly when both *static-* and *dynamic-coupling* mechanisms can be invoked. Absorption and emission spectra of various Yb(III) complexes have been investigated recently with the help of ab-initio multi-reference calculations,[35,36] revealing the importance of the CF splitting on the optical properties and the thermal dependence of the measured spectra. However, compared to the experimental data, numerical agreement was not achieved in term of calculated intensities as the active spaces used in these multi-reference calculations where only restricted to the strongly localized $4f$ electrons. Indeed, to properly calculate the transition dipole moments associated to the $4f$ transitions (both electric and magnetic dipole moments), one needs to take into account the effects

due to the mixing of the $4f^{13}$ electronic configurations with the excited ones such as the $4f^{12}5d^{1}$. To this purpose, we present herein an *ab-initio* study of the CD spectra of $[Yb(DOTMA)]^-$ that takes advantage of recent development allowing the calculation of rotatory strengths in length representation from multi-configurational calculations including SOC effects.[37,38] The CD spectrum obtained with this approach reproduce the experimental spectra and reveals the importance of breaking the parity rule in the calculated wavefunction for the interpretation of chiroptical properties in Yb(III) complexes.

2 Computational Details

The probability of absorbing a right and a left photon from an initial state i to a final state f is proportional to the rotatory strength R_{if}. In the case of an isotropic sample, R_{if} corresponds to the imaginary part of the scalar product between the ED transition moments $\boldsymbol{\mu}_{if}$ and the magnetic dipole (MD) transition moments $\mathbf{m}_{fi}$, and is expressed in the dipole-length representation as follows:

$$R_{if} = \mathrm{Im}\left[\langle i|\hat{\boldsymbol{\mu}}|f\rangle \cdot \langle f|\hat{\mathbf{m}}|i\rangle\right] \tag{1}$$

where $\hat{\mu} = -e\sum_i r_i$ is the ED operator and $\hat{m} = \frac{e\hbar}{2m_e}\sum_u(\hat{L}_u + g_e\hat{S}_u)$ corresponds to the MD operator with the orbital ($\hat{L}_u$) and spin ($\hat{S}_u$) angular momentum operators for a direction u of the magnetic field. We have recently shown that when the SOC is sizable, it is important to take into account the orbital angular momentum in addition to the spin angular momentum, as it can bring additional intensity into the magnetic transition dipole moments.[37] The use of the dipole-length formalism in Equation 1 leads to origin-dependent results, however, our previous work[37] and others[39,40] have shown that the origin dependence is not pronounced with the use of a good quality basis sets and the centering of mass or centering of nuclear charge coordinates. We also verified that a small displacement of the gauge origin does not drastically modify the results (see Table S3). Rotatory strengths were calculated at 0 K. To mimic the influence of the temperature, a Boltzmann averaging of the calculated rotatory strengths was carried out using the corresponding calculated energies given in Table S2 (see SI for details). In order to compare with the experimental data, the rotatory strengths were calculated with Equation 1 and then scaled with the following Gaussian function:

$$g(E) = \frac{1}{\sigma\sqrt{\pi}}\,\mathrm{e}^{\left(\frac{-(\Delta E)^2}{\sigma^2}\right)} \tag{2}$$

The *ab-initio* CD spectra were thus obtained as the superposition of all the Gaussian curves. If not stated otherwise, the Gaussian broadening was performed with a σ value of 0.01 eV (ca. 81 cm^{-1}).

The calculated CD spectra of $[Yb(DOTMA)]^-$ were performed on three different structures labelled NMR, PBE and PBE0, which correspond to structures determined experimentally by NMR,[26,41] and optimized with the help of density functional theory (DFT) calculations using the PBE[42,43] (Perdew-Burke-Ernzrhof) functional from the generalized gradient approximation (GGA) and its hybrid version PBE0,[44,45] respectively. The NMR structure was determined with

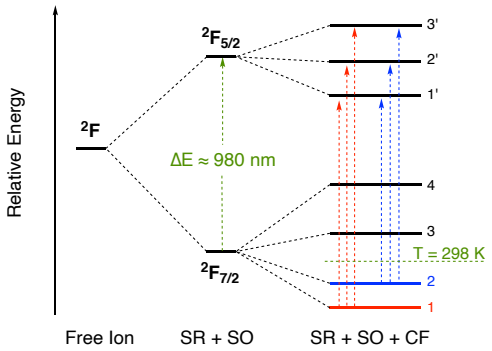

Figure 1: Schematic diagram of the energies of the lowest scalar relativistic (SR) and spin-orbit (SO) states of a $4f^{13}$ complex with the crystal-field (CF) interaction treated a posteriori. The two sets of arrow represent the thermally accessible transitions from the ground multiplet $^2F_{7/2}$ at room temperature.

the help of paramagnetic NMR analysis performed in methanol solution.[46] The structure corresponds to the major form in solution (R,R,R,R)-YbDOTMA and possesses a Λ helicity around the lanthanide ion. It is worth mentioning that the NMR structure is eight coordinated, whereas the minor form in solution (S,S,S,S)-YbDOTMA, also of Λ helicity, is hydrated and nine coordinated because of less steric hindrance from the ligands.[46] Di Bari *et al.* have shown that the CD spectrum of [Yb(DOTMA)]$^-$ recorded in methanol solution can be safely attributed to the major form,[25] and thus, only the Λ (R,R,R,R)-YbDOTMA configuration is investigated in this work. The DFT optimizations were performed using the NMR structure as a starting point, in order to keep the Λ (R,R,R,R)-YbDOTMA configuration. The choice of using a GGA functional and its hybrid version allowed us to slightly distort the structure (see Table S1) and evaluate the sensitivity of our CD calculations to structural changes. It might be noted that the structure of [Yb(DOTMA)]$^-$ is relatively rigid and thereby, larger structural changes were not expected. Theses DFT optimizations were carried out with the Amsterdam Density Functional software package,[47–49] along with the triplet-ζ plus polarization all-electron basis sets (TZP) for all atoms,[50] and with solvent effects taken into account by using the Conductor-Like Screening Model (COSMO) with the dielectric constants of methanol.[51] The transition dipole moments (TDMs) for the ED and MD moments were calculated using the state-average complete-active space (CAS) and restricted-active space (RAS) self-consistent field (SCF) approaches[52] as implemented in the OpenMolcas software package.[53] The calculations were first performed at the scalar level using the second-order Douglas-Kroll-Hess scalar relativistic Hamiltonian,[54–56] in combination with a triple-ζ plus polarization (TZP) basis set from the all electron atomic natural orbital relativistically contracted basis set (ANO-RCC).[57,58] The SOC was then introduced by a state interaction within the basis of spin-orbit free states using the restricted active space state interaction (RASSI) approach.[59] Dynamic correlation effects were treated using perturbation theory at the second order (CASPT2 and RASPT2).[60] In order to avoid the presence of intruder states, an imaginary shift of 0.75 au. with the standard IPEA shift value of 0.25 au.[61] were used. Solvent effects were included via the Conductor Polarizable Continuum Model (C-PCM).[62,63] The nature of the wavefunction was analyzed by using natural orbitals (NOs) that were directly obtained from the multiconfigurational wave functions that include SOC effects,[64–66] while natural bond orbital (NBO) analyses

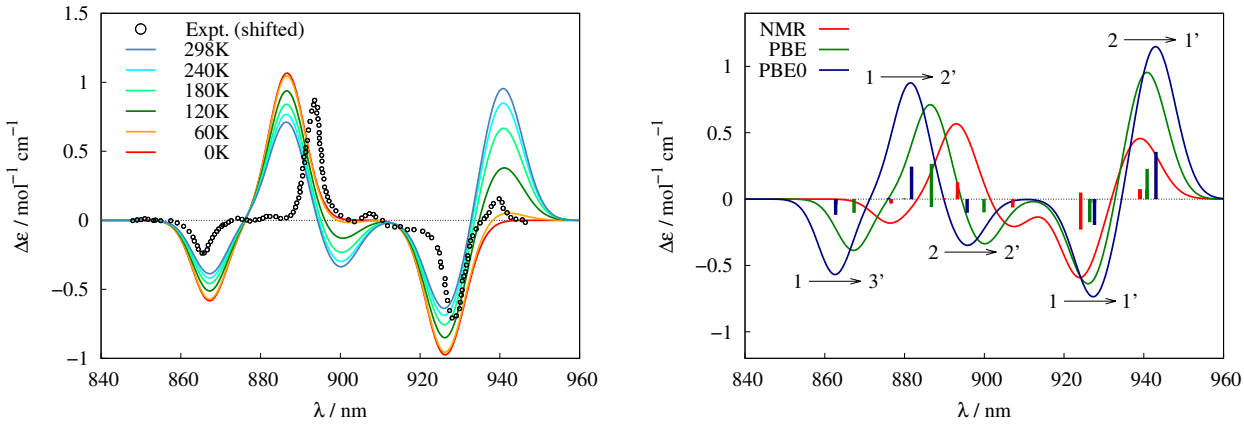

Figure 2: Calculated circular dichroism spectra of $[Yb(DOTMA)]^-$ as a function of the temperature using the PBE structure (left) and as a function of the structure at room temperature (right). The experimental spectrum at 298 K was generated using data extracted from Reference 25 and, for the purpose of comparison, has been shifted by -590 cm^{-1}.

were performed with the NBO6.0[67] program on the scalar relativistic wavefunctions without the h functions in the basis set of the Yb(III) centers.

The multi-configurational calculations employed a combination of CASSCF, RASSCF and RASCI wavefunction calculations. The influence of the $4f$ configurations was calculated at the CAS(13,7)SCF level, where the active space corresponded to the 13 electrons of the Yb(III) ion spanning the seven $4f$ orbitals. In this case, the state-average calculation included the 7 doublet spin states arising from the $4f^{13}$ electronic configuration. The influence of the $5d$ orbitals was investigated within a two-steps procedure combining complete and restricted active spaces. In this work, we use the RAS[n,l,m,i,j,k] notation where i, j and k correspond to the number of orbitals in the RAS2, RAS1 and RAS3 spaces, respectively, n is the number of electrons in the RAS2 space, and l and m are the number of holes and particules created in the RAS1 and RAS3 spaces, respectively. First, a RAS[13,0,1,0,7,5]SCF calculation, including 252 doublet spin states was performed on top of the previous CAS(13,7)SCF wavefunction to optimize the $5d$ orbitals. This RASSCF calculation allowed single excitation in the RAS3 space containing the five $5d$ orbitals of the Yb(III) ion. The $4f$ and $5d$ optimized orbitals were then used for a RAS[13,0,2,0,7,5]CI calculation (i.e. without orbital optimization), allowing double excitations in the RAS3 space, and performed on the lowest 7 doublet spin states. This computational strategy was recently applied for the calculations of the circularly polarized luminescence spectrum of $[Eu(DPA)_3]^{3-}$ and $[Yb(L)_3]^{3-}$ with L = tridentate amide ligand.[37,38]

3 Results and Discussion

The $4f^{13}$ electronic configuration of the Yb(III) ion gives rise at the scalar level to a ground term ^2F, which is then split by the SOC into to two $^{2S+1}L_J$ terms, namely $^2F_{7/2}$ and $^2F_{5/2}$ (see Figure 1). The transition between these two multiplets falls in the NIR region at ca. 980 nm. In $[Yb(DOTMA)]^-$, the degeneracy of the two multiplets is then lifted by the CF interaction into

four and three Kramers doublets, respectively. The magnitude of the splitting of the multiplets depends on the intensity of the CF. Therefore, at room temperature the CD spectrum of the Yb(III) based complexes can exhibit from 3 to 12 bands depending on the Boltzmann population of the excited states of the ground multiplet. Indeed, the experimental CD spectrum of $[Yb(DOTMA)]^-$ revealed 5 CD bands at 193 and 298 K with intensities that vary with the change of temperature (see Figure S1 of the SI), suggesting excitations from the lowest two Kramers doublet states.[25]

The calculated CD spectrum of $[Yb(DOTMA)]^-$, obtained at the RASPT2 level for the PBE structure, is shown in the left hand side of the Figure 2 and is compared to the experimental spectrum. The calculated spectrum reproduces nicely the shape of the experimental one with the alternance of negative and positive CD bands, but is overall blue shifted by ca. 600 cm^{-1} (see Table 1). At 0K, the calculated spectrum exhibits three major bands at 867, 886 and 926 nm that correspond to transitions from the ground state (GS, labelled **1** in Figure 1) to the three excited states (ES) of the $^2F_{5/2}$ multiplet **3'**, **2'** and **1'**, respectively (see Table 1). In comparison, these three bands were measured at 918, 946 and 980 nm, respectively. The increase of the temperature leads to the apparition of two new CD bands centered at 900 and 940 nm, while the intensity of the three other bands decreases. The two additional CD bands correspond to excitations from the first excited Kramers doublet of $^2F_{7/2}$ multiplet (labelled **2** in Figure 1), calculated at 165 cm^{-1} above the GS, into the higher in energy ES **2'** and **1'**, respectively. Interestingly, one should expect another additional CD bands. However, the third transition is calculated at 880 nm and is hidden by the transition calculated at 886 nm (**1** → **2'**), which bares a much larger rotatory strengths (see Table 1). The presence of a low-lying excited state is mandatory to rationalize the experimental spectrum. However, the intensity of the CD bands arising from this excited state **2** are calculated too large compared to the experimental ones, suggesting that either the energy gap ΔE_{1-2} is underestimated or the TDMs are overestimated. As visible in Figures S2 - S4 in the SI, agreement with the experimental spectrum is only achieved when both the $4f$ and the $5d$ orbitals are included in the active space in combination with dynamical correlation (RAS[13,0,2,0,7,5]CI-PT2 results). In comparison with the result obtained with only the $4f$ orbitals in the active space, the presence of both $4f$ and $5d$ orbitals allows to break the parity rule by mixing in the wavefunction $4f^{13}$ and $4f^{12}5d^1$ configurations. This admixture of configurations is required to obtain the proper GS, but also to obtain ED transition moments in the right order of magnitude.

In order to evaluate the influence of structural parameters on the CD properties, the CD spectrum of $[Yb(DOTMA)]^-$ was also calculated for two other structures, namely PBE0 and NMR, and the results are presented in the right hand side of Figure 2. Interestingly, one can observed that the calculated CD spectra are slightly blue shifted when going from the NMR to the PBE0 structures; this shift being more pronounced at lower wavelengths. The geometrical differences between the three structures are resumed in SI (Table S1 and Figure 3). When going from the structure characterized by NMR to the PBE0 one, one observes a contraction of the macrocycle DOTMA with shorter Yb-O and Yb-N bond lengths. This contraction of the molecule does not drastically modify the calculated electronic structure (see Table S2 in SI). The first ES (**2**) is only slightly destabilized by 10 cm^{-1} with the PBE0 structure, while the largest deviation is found for the ES **3'** which is more destabilized (ca. 170 cm^{-1}) with the PBE0 structure compared to the NMR one.

As shown in Table 2, the increase in magnitude of the CD bands between the different structures investigated results only from an increase of the ED moments and not from the MD moments.

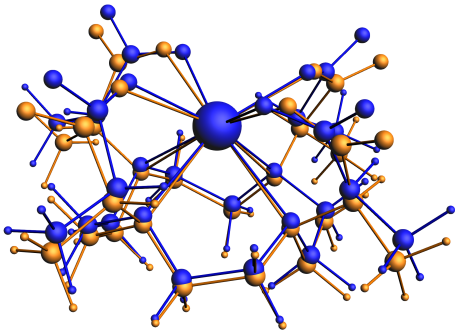

Figure 3: Overlay of the structures obtained from the NMR analysis[26] (orange) and from the DFT structural optimization using the PBE0 functional (blue).

This result is related to the amount of $4d^{(n-1)}5d$ configurations mixed into the wavefunction. To probe the contribution of these configurations, the population of the natural orbitals (NOs) of the SOC GS and the results of a natural population analysis (NPA) performed on the state-average scalar orbitals are given in Table 3, while the NOs are plotted in Figure 4. The occupation of the NOs for the SO GS are barely affected with the change of structure, with a minor decrease of the $4f$ orbital occupations in favor of the occupation of the $5d$ orbitals when going from NMR to PBE0. This trend is more pronounced with the NPA analysis, where the sum of the occupation numbers of the $5d$ orbitals increases from 0.56 to 0.68 electrons for the NMR and PBE0 structures, respectively. Overall, the contraction of the DOTMA macrocycle leads to a slight increase of the

Table 1: Calculated wavelength (λ, nm) and energy gap (ΔE, cm^{-1}), rotatory strengths (R, $\times 10^{-40}$ cgs) and absorption dissymmetry factor[a] (g_{abs}) at the RAS level of calculations for three different structures investigated.

	Expt.	NMR			PBE			PBE0		
	λ / ΔE	λ / ΔE	R	g_{abs}	λ / ΔE	R	g_{abs}	λ / ΔE	R	g_{abs}
1 → 1'	980	924	-0.260	-0.213	926	-0.296	-0.085	927	-0.331	-0.062
	10204	10818			10795			10781		
1 → 2'	946	893	0.240	0.539	886	0.310	0.242	881	0.366	0.168
	10570	11198			11278			11342		
1 → 3'	918	875	-0.083	-0.976	867	-0.166	-1.206	862	-0.236	-1.065
	10893	11423			11531			11592		
2 → 1'	-	938	0.516	1.100	940	0.997	0.591	943	1.231	0.454
		10653			10630			10605		
2 → 2'	-	906	-0.219	-1.023	900	-0.341	-0.786	895	-0.358	-0.601
		11033			11113			11166		
2 → 3'	-	888	0.025	0.140	880	0.023	0.078	876	0.035	0.065
		11258			11366			11416		

[a] $g_{abs} = 4 \cdot R/D$, with $D = |\mu|^2 + |m|^2$. R, $|\mu|^2$ and $|m|^2$ are in the same units of $esu^2\ cm^2$.

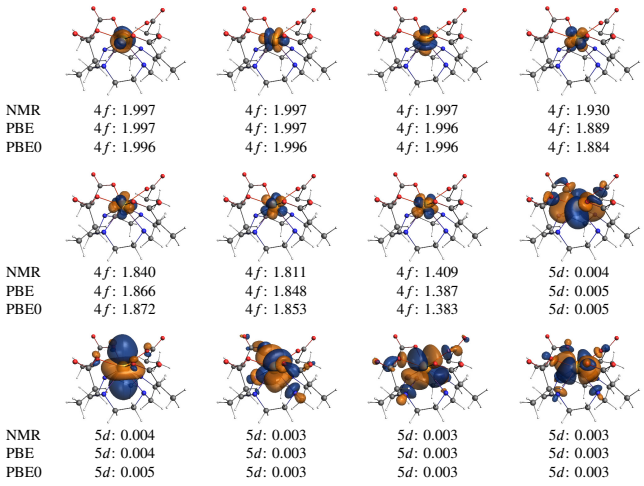

Figure 4: Selected Natural orbitals (NOs) of the SO GS of $[Yb(DOTMA)]^-$ calculated at the RAS[13,0,2,0,7,5]CI-PT2-SO level. Iso-surface value = ± 0.03 au. The occupation numbers of the corresponding NOs for the three different structures are given for comparison.

mixing of $4d^{(n-1)}5d$ configurations into the wavefunction, which is characterized by an increase of the $5d$ orbital populations. Despite its small magnitude, this increase of the $5d$ populations leads to an increase of the ED moments, and hence, the calculated rotatory strengths. Additionally, the increase of the calculated ED moments leads to a decrease of the calculated absorption dissymmetry factors (see Table 1), as g_{abs} corresponds to the ratio of $4 \cdot \boldsymbol{R}$ by the sum of the square of the dipole moments. For the **1** → **2'** transition, the RASPT2 calculations gave g_{abs} of 0.54, 0.27 and 0.17 for the NMR, PBE and PBE0 structures, respectively. These values compares relatively well with the experimental of 0.25 was measured at 946 nm.[25]

4 Conclusion

Overall, the combination of (i) breaking the parity rule with the mixing of $4f^{13}$ and $4f^{12}5d^1$ electronic configurations in the wavefunction, (ii) the inclusion of dynamical correlation and (iii) of spin-orbit coupling allowed us to properly reproduced the CD spectrum of the $[Yb(DOTMA)]^-$

Table 2: Calculated squared value of the electric ($|\mu|^2$, $\times 10^{-40}$ cgs) and magnetic ($|m|^2$, $\times 10^{-40}$ cgs) transition dipole moments. The gauge-origin corresponds to the center of mass of the complex (0.0,0.0,0.0).

	NMR		PBE		PBE0	
Transition	$\|\mu\|^2$	$\|m\|^2$	$\|\mu\|^2$	$\|m\|^2$	$\|\mu\|^2$	$\|m\|^2$
1 → **1'**	4.87	0.16	13.71	0.12	21.09	0.12
1 → **2'**	1.78	0.09	5.04	0.09	8.73	0.08
1 → **3'**	0.34	0.05	0.49	0.06	0.82	0.07

complex. We have shown that the subtle geometrical changes going with the contraction of the DOTMA ligand are responsible for a small but significant increase of the $4f^{12}5d^{1}$ electronic configurations in the wavefunction, and hence, are responsible for the increase of magnitude of the chiroptical properties. These results are in excellent agreement with the previous electrostatic models applied on $[Yb(DOTMA)]^{-}$,[28] and confirm that the optical activity in this dissymmetrical Yb(III) complex is controlled by a *static-coupling* mechanism. In a follow-up work, we aim to apply a similar ab-initio protocole in order to study the case where chiroptical properties are considered to be governed by a *dynamic-coupling* mechanism.

Acknowledgments

Authors acknowledge support from Agence Nationale de la Recherche (SMMCPL ANR-19-CE29-0012-02) and thank the French GENCI/IDRIS-CINES centers for high-performance computing resources. FG acknowledges the Stratégie d'Attractivité Durable (SAD18006 - LnCPLSMM) from the Région Bretagne for financial support. Pr. Jochen Autschbach from the State University of New York at Buffalo and Pr. Lorenzo Di Bari from the University of Pisa are acknowledged for their help and fruitful discussions.

Supporting Information

Additional calculated cd spectra, overlay of the different structures used for the calculations and energies of the Yb(III) states.

Table 3: Occupation numbers of the natural orbitals of the spin-orbit ground state (SO-GS NOs) and natural population analysis of the scalar ground state (SR-GS NPA) as a function of the structure used for the calculations.

Structure	SO-GS NOs	SR-GS NPA
NMR	$4f^{12.9820}5d^{0.0179}$	$4f^{12.98}5d^{0.56}6s^{0.18}6p^{0.01}6d^{0.07}$
PBE	$4f^{12.9809}5d^{0.0190}$	$4f^{12.96}5d^{0.63}6s^{0.17}6p^{0.02}6d^{0.09}$
PBE0	$4f^{12.9800}5d^{0.0199}$	$4f^{12.95}5d^{0.68}6s^{0.18}6p^{0.01}6d^{0.10}$

Table of Contents Graphics

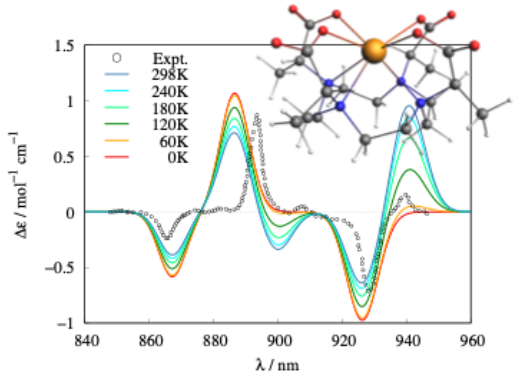

References

[1] A. de Bettencourt-Dias (Ed.), *Luminescence of Lanthanide Ions in Coordination Compounds and Nanomaterials*, John Wiley & Sons, Chichester, UK, 2014.

[2] S. V. Eliseeva, J.-C. G. Bünzli, *Chem. Soc. Rev.*, 2010, **39**, 189–227.

[3] M. C. Heffern, L. M. Matosziuk, T. J. Meade, *Chem. Rev.*, 2014, **114**, 4496–4539.

[4] R. Carr, N. H. Evans, D. Parker, *Chem. Soc. Rev.*, 2012, **41**, 7673–7686.

[5] J.-C. G. Bünzli, S. V. Eliseeva, *Chem. Sci.*, 2013, **4**, 1939–1949.

[6] C. Yang, A. M. Kaczmarek, K. Folens, G. Du Laing, H. Vrielinck, S. Khelifi, K. Li, R. Van Deun, *Mater. Chem. Front.*, 2019, **3**, 579–586.

[7] F. Zinna, M. Pasini, F. Galeotti, C. Botta, L. Di Bari, U. Giovanella, *Adv. Funct. Mater*, 2017, **27**, 1603719.

[8] F. Zinna, U. Giovanella, L. Di Bari, *Adv. Mater*, 2015, **27**, 1791–1795.

[9] A. de Bettencourt-Dias, *Lanthanides: Electronic Structure*, R. A. Scott (Ed.), American Cancer Society, 2012.

[10] M. Dolg (Ed.), *Computational Methods in Lanthanide and Actinide Chemistry*, John Wiley & Sons, Ltd, Chichester, UK, 2015.

[11] M. Atzori, K. Dhbaibi, H. Douib, M. Grasser, V. Dorcet, I. Breslavetz, K. Paillot, O. Cador, G. L. J. A. Rikken, B. Le Guennic, J. Crassous, F. Pointillart, C. Train, *J. Am. Chem. Soc.*, 2021, **143**, 2671–2675.

[12] M. Abdus Subhan, T. Suzuki, S. Kaizaki, *J. Chem. Soc., Dalton Trans.*, 2001, 492–497.

[13] G. Castro, M. Regueiro-Figueroa, D. Esteban-Gomez, P. Perez-Lourido, C. Platas-Iglesias, L. Valencia, *Inorg. Chem.*, 2016, **55**, 3490–3497.

[14] O. Cador, B. Le Guennic, F. Pointillart, *Inorg. Chem. Front.*, 2019, **6**, 3398.

[15] C. L. Maupin, D. Parker, J. A. G. Williams, J. P. Riehl, *J. Am. Chem. Soc.*, 1998, **120**, 10563–10564.

[16] R. S. Dickins, J. A. K. Howard, C. L. Maupin, J. M. Moloney, D. Parker, J. P. Riehl, G. Siligardi, J. A. G. Williams, *Chem. Eur. J.*, 1999, **5**, 1095–1105.

[17] C. L. Maupin, R. S. Dickins, L. G. Govenlock, C. E. Mathieu, D. Parker, J. A. G. Williams, J. P. Riehl, *J. Phys. Chem. A*, 2000, **104**, 6709–6717.

[18] S. Di Petro, L. Di Bari, *Inorg. Chem.*, 2012, **51**, 12007–12014.

[19] M. Górecki, L. Carpita, L. Arrico, F. Zinna, L. Di Bari, *Dalton Trans.*, 2018, **47**, 7166–7177.

[20] M. Lelli, L. Di Bari, *Dalton Trans.*, 2019, **48**, 882–890.

[21] F. Zinna, L. Arrico, L. Di Bari, *Chem. Commun.*, 2019, **55**, 6607–6609.

[22] Y. Yamada, D. Koori, K. Mori, Y. Oshikawa, *J. Coord. Chem.*, 2016, **69**, 3735–3744.

[23] F. Gonçalves e Silva, O. L. Malta, C. Reinhard, H.-U. Güdel, C. Piguet, J. E. Moser, J.-C. G. Bünzli, *J. Phys. Chem. A*, 2002, **106**, 1670–1677.

[24] M. Abdus Subhan, Y. Hasegawa, T. Suzuki, S. Kaizaki, Y. Shozo, *Inorganica Chimica Acta*, 2009, **362**, 136–142.

[25] L. Di Bari, G. Pintacuda, P. Salvadori, *J. Am. Chem. Soc.*, 2000, **122**, 5557–5562.

[26] L. Di Bari, G. Pintacuda, P. Salvadori, R. S. Dickins, D. Parker, *J. Am. Chem. Soc.*, 2000, **122**, 9257–9264.

[27] L. Di Bari, G. Pescitelli, A. D. Sherry, M. Woods, *Inorg. Chem.*, 2005, **44**, 8391–8398.

[28] R. Berardozzi, L. Di Bari, *Chem. Phys. Chem.*, 2015, **16**, 2868–2875.

[29] S. F. Mason, R. D. Peacock, B. Stewart, *Mol. Phys.*, 1975, **30**, 1829–1841.

[30] F. S. Richardson, T. R. Faulkner, *J. Chem. Phys.*, 1982, **76**, 1595–1606.

[31] B. R. Judd, *Phys. Rev.*, 1962, **127**, 750–761.

[32] G. S. Ofelt, *J. Chem. Phys.*, 1962, **37**, 511–520.

[33] F. Zinna, L. Di Bari, *Chirality*, 2015, **27**, 1–13.

[34] S. Jurinovich, G. Pescitelli, L. Di Bari, B. Mennucci, *Phys. Chem. Chem. Phys.*, 2014, **16**, 16407–16418.

[35] A. Rodriguez-Rodriguez, A. Arnosa-Prieto, I. Brandariz, D. Esteban-Gomez, C. Platas-Iglesias, *J. Phys. Chem. A*, 2020, **124**, 1362–1371.

[36] D. Esteban-Gomez, L. Büldt, P. Perez-Lourido, L. Valencia, M. Seitz, Platas-Iglesias, *Inorg. Chem.*, 2019, **58**, 3732–3743.

[37] F. Gendron, B. Moore II, O. Cador, F. Pointillart, J. Autschbach, B. Le Guennic, *J. Chem. Theory Comput.*, 2019, **15**, 4140–4155.

[38] F. Gendron, S. Di Pietro, L. Abad Galán, F. Riobé, V. Placide, L. Guy, F. Zinna, L. Di Bari, A. Bensalah-Ledoux, Y. Guyot, G. Pilet, F. Pointillart, B. Baguenard, S. Guy, O. Cador, O. Maury, B. Le Guennic, *Inorg. Chem. Front.*, 2021, **8**, 914–921.

[39] L. K. Sørensen, M. Guo, R. Lindh, M. Lundberg, *Mol. Phys.*, 2017, **115**, 174–189.

[40] P. J. Lestrange, F. Egidi, X. Li, *J. Chem. Phys.*, 2015, **143**, 234103.

[41] L. Di Bari, M. Lelli, G. Pintacuda, G. Pescitelli, F. Marchetti, P. Salvadori, *J. Am. Chem. Soc.*, 2003, **125**, 5549–5558.

[42] J. P. Perdew, K. Burke, M. Ernzerhof, *Phys. Rev. Lett.*, 1996, **77**, 3865–3868.

[43] J. P. Perdew, K. Burke, M. Ernzerhof, *Phys. Rev. Lett.*, 1997, **78**, 1396.

[44] M. Ernzerhof, G. E. Scuseria, *J. Chem. Phys.*, 1999, **110**, 5029–5036.

[45] C. Adamo, V. Barone, *J. Chem. Phys.*, 1999, **110**, 6158–6170.

[46] L. Di Bari, G. Pintacuda, P. Salvadori, *Eur. J. Inorg. Chem.*, 2000, 75–82.

[47] G. te Velde, F. M. Bickelhaupt, E. J. Baerends, S. J. A. van Gisbergen, C. Fonseca Guerra, J. G. Snijders, T. Ziegler, *J. Compt. Chem.*, 2001, **22**, 931–967.

[48] C. Fonseca Guerra, J. G. Snijders, G. te Velde, E. J. Baerends, *Theor. Chem. Acc.*, 1998, **99**, 391.

[49] E. J. Baerends, T. Ziegler, A. J. Atkins, J. Autschbach, D. Bashford, O. Baseggio, A. Bérces, F. M. Bickelhaupt, C. Bo, P. M. Boerritger, L. Cavallo, C. Daul, D. P. Chong, D. V. Chulhai, L. Deng, R. M. Dickson, J. M. Dieterich, D. E. Ellis, M. van Faassen, A. Ghysels, A. Giammona, S. J. A. van Gisbergen, A. Goez, A. W. Götz, S. Gusarov, F. E. Harris, P. van den Hoek, Z. Hu, C. R. Jacob, H. Jacobsen, L. Jensen, L. Joubert, J. W. Kaminski, G. van Kessel, C. König, F. Kootstra, A. Kovalenko, M. Krykunov, E. van Lenthe, D. A. McCormack, A. Michalak, M. Mitoraj, S. M. Morton, J. Neugebauer, V. P. Nicu, L. Noodleman, V. P. Osinga, S. Patchkovskii, M. Pavanello, C. A. Peeples, P. H. T. Philipsen, D. Post, C. C. Pye, H. Ramanantoanina, P. Ramos, W. Ravenek, J. I. Rodríguez, P. Ros, R. Rüger, P. R. T. Schipper, D. Schlüns, H. van Schoot, G. Schreckenbach, J. S. Seldenthuis, M. Seth, J. G. Snijders, M. Solà, S. M., M. Swart, D. Swerhone, G. te Velde, V. Tognetti, P. Vernooijs, L. Versluis, L. Visscher, O. Visser, F. Wang, T. A. Wesolowski, E. M. van Wezenbeek, G. Wiesenekker, S. K. Wolff, T. K. Woo, A. L. Yakovlev, *ADF2017, SCM, Theoretical Chemistry, Vrije Universiteit, Amsterdam, The Netherlands, https://www.scm.com*, 2017.

[50] E. van Lenthe, E. J. Baerends, *J. Comput. Chem.*, 2003, **24**, 1142–1156.

[51] C. C. Pye, T. Ziegler, *Theor. Chem. Acc.*, 1999, **101**, 396–408.

[52] B. O. Roos, P. R. Taylor, P. E. M. Siegbahn, *Chem. Phys.*, 1980, **48**, 157–173.

[53] I. Fdez. Galván, M. Vacher, A. Alavi, C. Angeli, F. Aquilante, J. Autschbach, J. J. Bao, S. I. Bokarev, N. A. Bogdanov, R. K. Carlson, L. F. Chibotaru, J. Creutzberg, N. Dattani, M. G. Delcey, S. S. Dong, A. Dreuw, L. Freitag, L. M. Frutos, L. Gagliardi, F. Gendron, A. Giussani, L. González, G. Grell, M. Guo, C. E. Hoyer, M. Johansson, S. Keller, S. Knecht, G. Kovačević, E. Källman, G. Li Manni, M. Lundberg, Y. Ma, S. Mai, J. P. Malhado, P. Å. Malmqvist, P. Marquetand, S. A. Mewes, J. Norell, M. Olivucci, M. Oppel, Q. M. Phung, K. Pierloot, F. Plasser, M. Reiher, A. M. Sand, I. Schapiro, P. Sharma, C. J. Stein, L. K. Sørensen, D. G. Truhlar, M. Ugandi, L. Ungur, A. Valentini, S. Vancoillie, V. Veryazov, O. Weser, T. A. Wesołowski, P.-O. Widmark, S. Wouters, A. Zech, J. P. Zobel, R. Lindh, *J. Chem. Theory Comput.*, 2019, **15**, 5925–5964.

[54] M. Douglas, N. M. Kroll, *Ann. Phys.*, 1974, **82**, 89–155.

[55] B. A. Hess, *Phys. Rev. A*, 1985, **32**, 756–763.

[56] B. A. Hess, *Phys. Rev. A*, 1986, **33**, 3742–3748.

[57] P.-O. Widmark, P.-Å. Malmqvist, B. O. Roos, *Theor. Chim. Acta*, 1990, **77**, 291–306.

[58] B. O. Roos, R. Lindh, P.-Å. Malmqvist, V. Veryazov, P.-O. Widmark, *J. Phys. Chem. A*, 2004, **108**, 2851–2858.

[59] P.-A. Malmqvist, B. O. Roos, B. Schimmelpfennig, *Chem. Phys. Lett.*, 2002, **357**, 230–240.

[60] K. Andersson, P.-Å. Malmqvist, B. O. Roos, A. J. Sadlev, K. Wolinski, *J. Phys. Chem.*, 1990, **94**, 5483–5488.

[61] J. P. Zobel, J. J. Nogueira, L. González, *Chem. Sci.*, 2017, **8**, 1482.

[62] M. Cossi, N. Rega, G. Scalmani, V. Barone, *J. Chem. Phys.*, 2001, **114**, 5691.

[63] V. Barone, M. Cossi, *J. Phys. Chem. A*, 1998, **102**, 1995–2001.

[64] F. Gendron, D. Páez-Hernández, F.-P. Notter, B. Pritchard, H. Bolvin, J. Autschbach, *Chem. Eur. J.*, 2014, **20**, 7994–8011.

[65] F. Gendron, H. Bolvin, J. Autschbach in *Organometallic Magnets*, of *Topics in Organometallic Chemistry*, V. Chandrasekhar, F. Pointillart (Eds.), Springer, Berlin, Heidelberg, 2018.

[66] F. Gendron, B. Pritchard, H. Bolvin, J. Autschbach, *Dalton Trans.*, 2015, **44**, 19886–19900.

[67] E. D. Glendening, C. R. Landis, F. Weinhold, *J. Comput. Chem.*, 2013, **34**, 1429–1437.